ORIGINAL ARTICLE

Mechanical Properties and Energy Absorption of Integrated AlSi10Mg Shell Structures with BCC Lattice Infill

Yingchun Bai[1*] , Jiayu Gao[1], Chengxiang Huang[1] and Yue Li[1]

Abstract

Shell-infill structures comprise an exterior solid shell and an interior lattice infill, whose closed features yield superior comprehensive mechanical performance and light weight. Additive manufacturing (AM) can ensure the fabrication of complex structures. Although the mechanical behaviors of lattice structures have been extensively studied, the corresponding mechanical performances of integrated-manufactured shell structures with lattice infills should be systematically investigated due to the coupling effect of the exterior shell and lattice infill. This study investigated the mechanical properties and energy absorption of AlSi10Mg shell structures with a body-centered cubic lattice infill fabricated by AM. Quasi-static compressive experiments and corresponding finite element analysis were conducted to investigate the mechanical behavior. In addition, two different finite element modeling methods were compared to determine the appropriate modeling strategy in terms of deformation behavior. A study of different parameters, including lattice diameters and shell thicknesses, was conducted to identify their effect on mechanical performance. The results demonstrate the mechanical advantages of shell-infill structures, in which the exterior shell strengthens the lattice infill by up to 2.3 times in terms of the effective Young's modulus. Increasing the infill strut diameter can improve the specific energy absorption by up to 1.6 times.

Keywords Shell-infill structure, Body center cubic (BCC), Additive manufacturing, Compression properties, Energy absorption

1 Introduction

Shell-infill structures generally comprise exterior solid shells and interior porous infill structures, whose closed features can generate superior mechanical performance, such as high stiffness-to-weight ratio, strength-to-weight ratio, energy and sound absorption capacities [1–3]. Compared with conventional pure solid structures, shell-infill structures can concurrently coordinate the design of the overall structure and interior infill configuration with

greater design freedom, thereby maximizing the mechanical performance and improving the light weight [4–6].

For shell-infill structures, many studies have focused on the infill configuration and investigated the effects of topology and geometric size on the structural mechanical properties. Li [7] designed a honeycomb aluminum cell with different unit lengths to investigate the influence of the relative position on the energy absorption capacity. Zhang [8] compared the crushing performance of shell structures with triangular, hexagonal, and negative Poisson's ratio (NPR) structures as porous infills; a huge difference was found in terms of energy absorption under both quasi-static compression and impact conditions. Zeng et al. [9, 10] discussed the differences in the failure modes of shell-infill structures by changing the corrugation angle during compression and three-point

*Correspondence:
Yingchun Bai
baiyc@bit.edu.cn
[1] National Engineering Research Center of Electric Vehicles, School of Mechanical Engineering, Beijing Institute of Technology, Beijing 100081, China

Bai *et al. Chinese Journal of Mechanical Engineering* (2023) 36:143

Page 2 of 13

bending experiments. Muchhala et al. [11] investigated the axial compressive deformation mechanism of ceno-sphere-reinforced closed-cell hybrid aluminum foams at different strain rates. Vengatachalam et al. [12] studied the initial yield response of closed-cell aluminum foams under both uniaxial and biaxial loadings. Cherniaev [13] analyzed the damage to sandwich panels with open-cell foam under impact to confirm the protective function of this type of structure. These types of shell structures with porous infills have been widely studied in terms of their compressive performance. Hu et al. [14] investigated the deformation, strength, and failure modes of woven textile sandwich composites (WTSCs). In addition to the infill configuration, Wang et al. [15, 16] also explored the buckling deformation mode of cylindrical shells under axial loads through experiments and numerical methods. Most structures mentioned above were fabricated by conventional manufacturing processes, such as stretching from honeycomb structures or casting for shell foam structures.

With the recent utilization of additive manufacturing (AM), structures with complicated geometries, such as shell-infill structures, can be manufactured, providing greater design freedom [17–19]. As a promising infill porous structure, the lattice structure can achieve superior mechanical or multifunctional properties while maintaining an extremely light weight [20]. Maconachie et al. [21] reviewed and summarized existing studies on lattice structures and provided design guidance for developing controllable mechanical properties. Body center cubic (BCC) structures are the most widely studied lattice type in terms of their mechanical response and elastoplastic deformation mechanism under quasi-static compression. Peng et al. [22] numerically analyzed the mapping relationship between the relative density and mechanical properties of four lattice structures, including the BCC structure. Li [23] investigated the tensile and compressive local stress distributions of stainless-steel BCC unit cells from a microscopic perspective. Smith et al. [24] also reported the same progressive failure mode of BCC structures under quasistatic compression and blast loading conditions. Merkt et al. [25] performed compression tests and found that lattices manufactured with titanium alloys demonstrated inferior energy absorption capacity compared to that of stainless steel. To control the deformation behavior, Maskery et al. [26] realized a gradient-density lattice along the loading direction to obtain progressive layer collapse while ensuring the same energy absorption capacity. Sufiiarov et al. [27] eliminated shear failure with a computationally generated variable density to strengthen the mechanical responses of lattice structures. Apart from the above mechanism-based design methods, topology optimization can also be used to design cellular patterns or configurations based on the design requirements. Xu et al. [28] employed topology optimization to obtain the material distribution for an improved BCC structure. Kang et al. [29] combined topology optimization and a multilattice structure construction strategy to design sandwich-structured cores.

Most of the abovementioned studies related to the BCC lattice have focused on the multifunctional design of pure lattice structures in terms of mechanical properties and energy absorption capacities. However, lattice structures are usually covered by thin exterior densified shells, which can effectively prevent early-stage excessive deformation and thus strengthen the load-carrying capacities [30, 31]. Cetin et al. [32–34] investigated the energy absorption capacity of lattice-filled thin-walled tubes under impact conditions and determined the corresponding effects of uniform- and graded-lattice infills. Liu et al. [35] investigated the mechanical behavior of lattice-filled thin-walled tubes with single and multiple cells, in which a pre-manufactured lattice infill was inserted into the thin-shell tubes to form an assembly. It is believed that the mechanical performance of this simple assembly is inferior because of the lack of mechanical joining between the two separate parts. The additively manufactured integrated shell-infill structure can effectively solve the above-mentioned problems and significantly enhance mechanical properties and energy absorption [36].

This study investigated additively manufactured integrated shell structures with BCC-type porous infill in terms of their mechanical properties and energy absorption capabilities from both experimental and numerical perspectives. The remainder of this paper is organized as follows. The details of the experimental specimen, testing scheme, and corresponding finite element model construction under quasi-static loading conditions are provided in Section 2. The experimental results for different strut diameters are presented and discussed in Section 3. Section 4 presents the finite element modeling strategy selection by comparing simulation results with experimental ones, based on which the shell thickness influnce is studied. Finally, some conclusions are drawn in Section 5.

2 Materials and Methods
2.1 Model Design
The corresponding infill configuration significantly influenced the mechanical responses and deformation modes for shell structures with lattice infill. In this study, a BCC lattice was selected as the porous infill because of its simple topology and manufacturability. Considering the selective laser melting (SLM) process, a unit BCC cell with
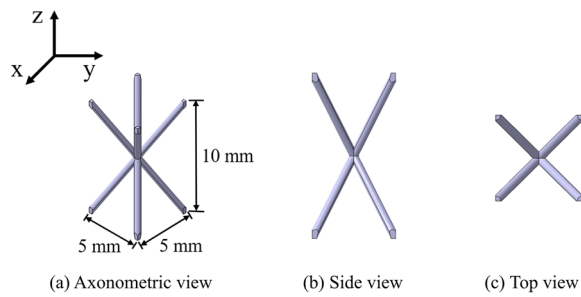
(a) Axonometric view   (b) Side view   (c) Top view

Figure 1 Model details of unit cell

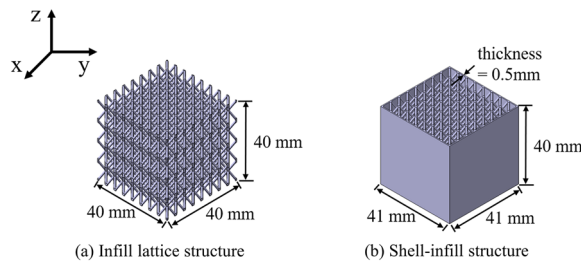(a) Infill lattice structure   (b) Shell-infill structure

Figure 2 Model details of integrated structure

dimensions of 5 mm × 5 mm × 10 mm was designed, as illustrated in Figure 1. The infill structure contained 8 × 8 × 4 BCC cells, and the infill lattice structure was enclosed by a thin shell with a thickness of 0.5 mm, as illustrated in Figure 2. For comparison, three different strut diameters for the infill lattices were designed: 0.5, 1.0, and 1.5 mm, and the corresponding relative densities of the lattice infill were 0.082, 0.172, and 0.301, respectively.

To obtain material parameters that are more consistent with the actual shell-infill structure, standard tensile samples were designed to obtain the parent material according to the ASTM E8 standard. Considering that the infill structure dominated a large portion of the structure, the standard tensile samples were manufactured in an oblique direction in accordance with the strut manufacturing direction of the designed shell-infill structure. The details of the specimen and printing direction are presented in Figure 3.

2.2 Materials and Fabrication

AlSi10Mg is a commonly used material for lightweight design and manufacturing and is also a widely developed AM material. All the specimens were prepared using AlSi10Mg powder with an average particle diameter of 35 μm. A BLT-S210 SLM machine with a laser power of 340 W was used. The scanning speed was set to 1400 mm/s, and the thickness of each layer was approximately 30 μm. To eliminate residual stress, all the samples were post-treated at a temperature of 280 ± 5 ℃ for 2 h. The printing direction of the shell-infill samples was
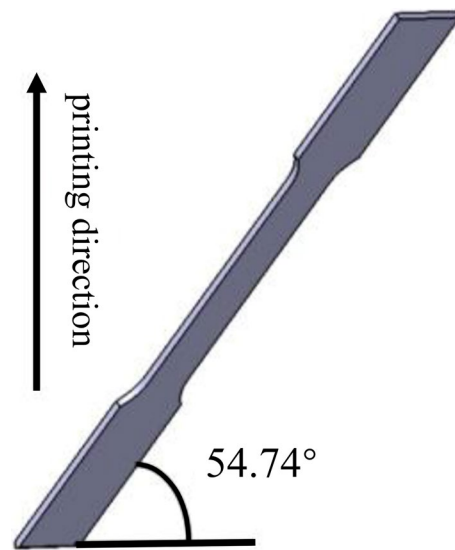

Figure 3 Standard tensile samples

parallel to the *z*-axis, as illustrated in Figure 2. The printing directions of the standard tensile samples are presented in Figure 3. All obtained samples are presented in Figure 4, and the sample details are presented in Table 1.

2.3 Experimental Test Scheme

Tensile tests of the single-strut and compression tests of the shell-infill structures were performed using a universal testing machine (WDW-200, TE). As illustrated in Figure 5, a uniaxial tensile test of a single strut with a diameter of 1.0 mm was conducted at a displacement rate of 1 mm/min according to the ASTM E8-15a standard. For the compression test, the loading direction was perpendicular to the top surface at a displacement rate of 0.5 mm/min in accordance with the ASTM E9-09 standard. A noncontact video extensometer (RTTS-100) was used to measure the deformation by tracing the relative displacement.

2.4 Tensile Results of Single Strut Sample

Figure 6 presents the stress-strain curve of the standard strut sample. All samples expire in the three stages of elasticity, yielding, and failure. The average value of the experimental data obtained from the two obliquely printed samples was utilized as the basic material parameter and simulation input curve for subsequent simulations, with Young's modulus of 66444.8 MPa and Poisson's ratio of 0.33.

For the finite element analysis, the obtained experimental nominal stress and strain were converted to true stress and strain [37]. The true strain is expressed as follows:

(a) Standard tensile samples for material characterization
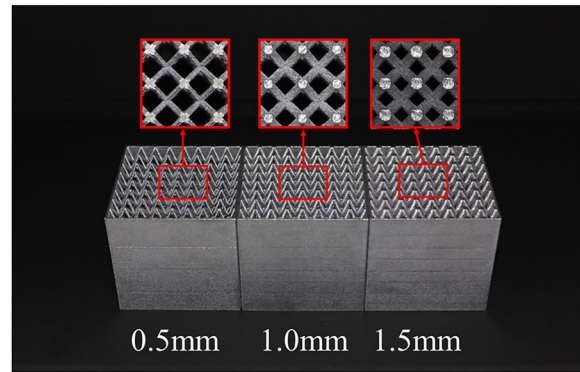
(b) Shell-infill samples

Figure 4 Additively manufactured experimental samples

Table 1 Geometry and mass information of shell-infill specimens

Strut diameter		0.5	1.0	1.5
Mass (g)		25.74	45.31	69.71
Length	Design value (mm)	41	41	41
	Actual value (mm)	41.35	41.37	41.32
	Error (%)	0.85	0.90	0.78
Width	Design value (mm)	41	41	41
	Actual value (mm)	41.38	41.52	41.44
	Error (%)	0.93	1.27	1.07
Height	Design value (mm)	40	40	40
	Actual value (mm)	39.75	39.79	39.85
	Error (%)	−0.63	−0.53	−0.38
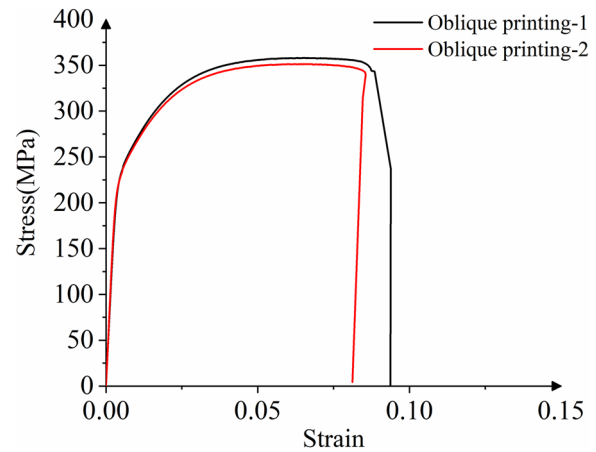
Figure 6 Stress-strain curve of tensile samples

$$\varepsilon = \ln(\varepsilon_{\text{nom}} + 1), \tag{1}$$

where ε_{nom} is the nominal strain, which can be obtained as

$$\varepsilon_{\text{nom}} = \frac{l}{l_0} - 1, \tag{2}$$

where l_0 is the original length, l is the current measured length, all can be obtained from the test. Considering the incompressibility of plastic deformation, the relationship between true stress and nominal stress is expressed as

$$\sigma = \sigma_{\text{nom}}(1 + \varepsilon_{\text{nom}}), \tag{3}$$

where σ is the true stress, and σ_{nom} is the nominal stress. As the strain obtained from the experimental data was the total strain of the samples rather than the plastic strain, it was necessary to decompose the total strain into
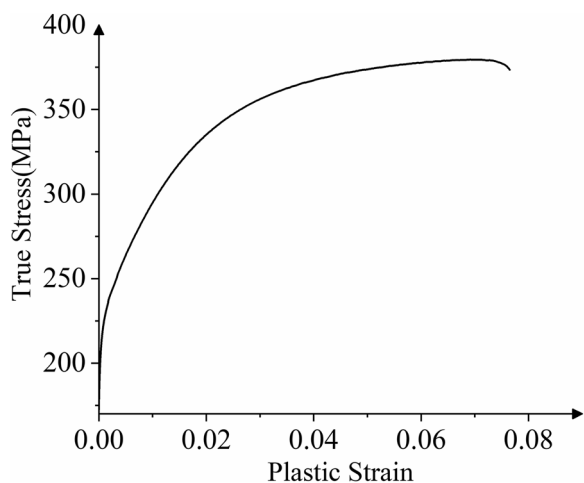

Figure 5 Experimental setup to measure uniaxial tension

Figure 7 True stress–strain curve obtained from simulation

elastic and plastic strain components. The plastic strain can be expressed as

$$\varepsilon^{\mathrm{pl}} = \varepsilon - \frac{\sigma}{E}, \tag{4}$$

where $\varepsilon^{\mathrm{pl}}$ represents plastic strain and E is the Young's modulus. The plastic strain and true stress curves are illustrated in Figure 7.

2.5 Finite Element Modeling Method
Shell or lattice structures can be simulated with well-developed finite element modeling approaches; however, this method is unsuitable for integrated shell-infill structures owing to the large geometric and material gradients. The coupling effect between the exterior shell and interior lattice significantly affects the mechanical properties and energy absorption. This study systematically investigated two finite element modeling approaches to select the most appropriate approach: a beam-shell type and a solid element type.

ABAQUS/EXPLICIT-6.16 software package was employed to build the corresponding finite element model. In the beam-shell type finite element model, shell elements (S4R) were used for the exterior shells, whereas beam elements (B31) were used for the infill lattices. The total number of beam elements was 24576, whereas that of the shell elements was 25600. Constraints were applied at the connection nodes between the beam and shell elements (Figure 8). Detailed partition modeling was adopted for the solid element model to ensure model accuracy owing to the inherently large geometric gradient. The finite element models with 0.5, 1.0, and 1.5 mm strut diameters have 706722, 743563, and 782292 C3D8R elements, respectively (Figure 9). The boundary conditions for the quasi-static analysis of both models are illustrated in Figure 10.

3 Experimental Results and Discussions
3.1 Experimental Results of Sample with Strut Diameter of 0.5 mm
The stress-strain curve of the shell-infill structure with a strut diameter of 0.5 mm is plotted in Figure 11. The compression history includes three typical stages: elastic damage, nonlinear damage, and densification. The elastic phase occurred before the exterior shell bulking, in which the stress demonstrated a linear and rapid increase until a peak was reached at the buckling stress threshold. Subsequently, the structure entered the nonlinear damage stage, and the load-bearing capability degenerated significantly with severe exterior shell buckling. With the collapse of the exterior shell, the stress of the entire structure reached the minimum value of the entire nonlinear stage, which was only 5% of the maximum stress value of the elastic stage (Figure 11(b)). The main load-bearing part was switched from the exterior shells to the BCC infill structure at this stage. The tearing between the exterior shells started from the bottom, and the destruction of the internal BCC structures resulted in the
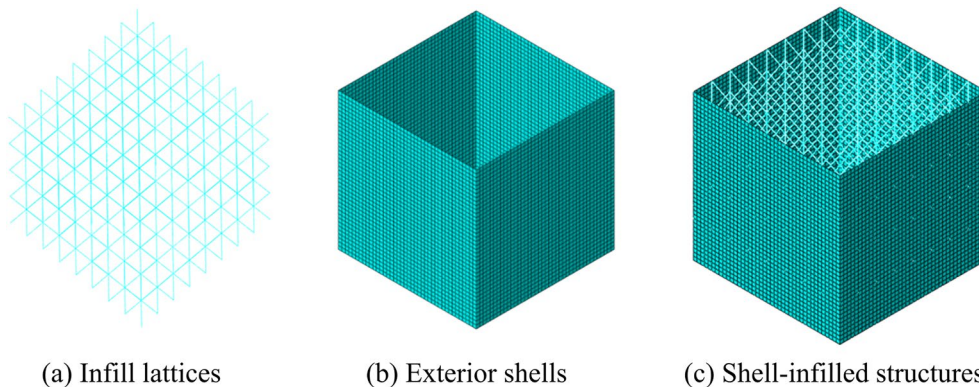

(a) Infill lattices　　(b) Exterior shells　　(c) Shell-infilled structures

Figure 8 Beam-shell type finite element model

geometry   mesh   geometry   mesh

(a) Unit cell   (b) Exterior shell

geometry   mesh

(c) Shell-infilled structures

Figure 9 Solid-type finite element model

Figure 11 Stress–strain curve of sample with 0.5-mm strut diameter
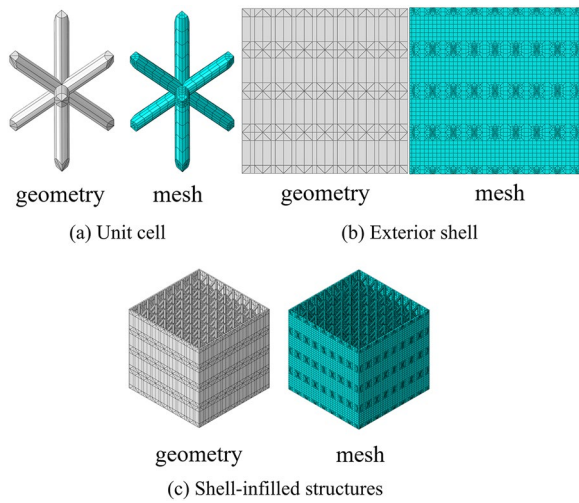
exterior shells in the lower half completely losing their load-bearing capacity. With an increase in the loading, the bottom of the upper half of the exterior shells was in full contact with the solid body; thus, the exterior shells became the main load-bearing part, causing the stress to reach the second peak, as illustrated in Figure 11(c). At this time, the tearing between the adjacent shells spread from the middle to the top. After buckling occurred, the middle of the structure expanded outward. It can also be noted that stress-strain curve has three smaller peaks for a strain range of 0.2–0.5, which is caused by the collapse of the BCC lattice infill.
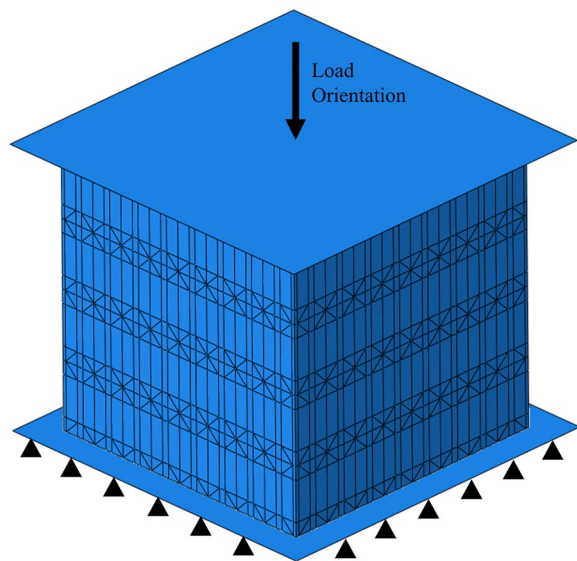

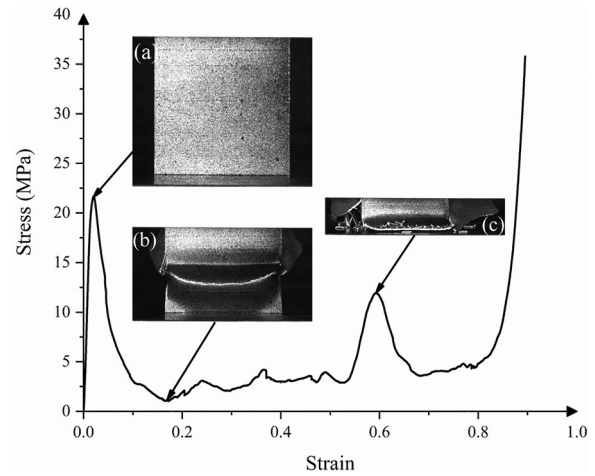**Figure 10** Boundary conditions for quasi-static analysis

Figure 12 presents the four other critical deformation modes. The first rupture occurred between adjacent shells in approximately half of the structure (Figure 12(a)), and the cracks gradually spread to the buckling parts of the shells (Figure 12(b)). As the damage intensified, lateral deformation resulted in the tearing of the adjacent shells (Figure 12(c)). Finally, the exterior shells completely lost their load-bearing capacity, and the structure entered the densification stage.

3.2 Experimental Results of Sample with Strut Diameter of 1.0 mm

As illustrated in Figure 13, four stress peaks were observed during deformation. The elastic stage of the 1.0-mm sample was similar to that of the 0.5-mm sample; however, the initial buckling position of the exterior shells of the 1.0-mm sample was lower at the beginning of the nonlinear damage stage (Figure 13(b)). The adjacent perpendicular shells were torn from each other, as illustrated in Figure 13(c), owing to stress concentration.
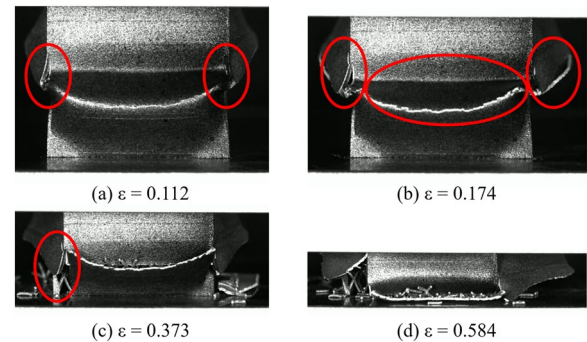

(a) ε = 0.112   (b) ε = 0.174

(c) ε = 0.373   (d) ε = 0.584

Figure 12 Critical deformations for sample with 0.5-mm strut diameter

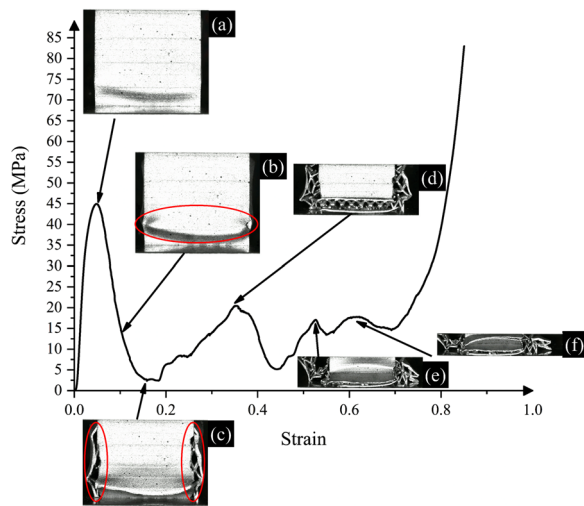**Figure 13** Stress–strain curve of sample with 1.0-mm strut diameter

Figure 14 Stress–strain curve of sample with 1.5-mm strut diameter

Subsequently, a second stress peak was observed after the exterior shell structure temporarily lost its load-bearing capability (Figure 13(d)). In Figure 13(e) and (f), the front and rear shells share load bearing with the internal BCC structures, leading to the third and fourth stress peaks. Based on these observations, the buckling of the exterior shells for the sample with a 0.5-mm strut diameter was more severe than that for the sample with a 1.0-mm strut diameter.

3.3 Experimental Results of Sample with Strut Diameter of 1.5 mm

Figure 14 presents the stress-strain curve of a sample with a strut diameter of 1.5 mm. Regarding the buckling
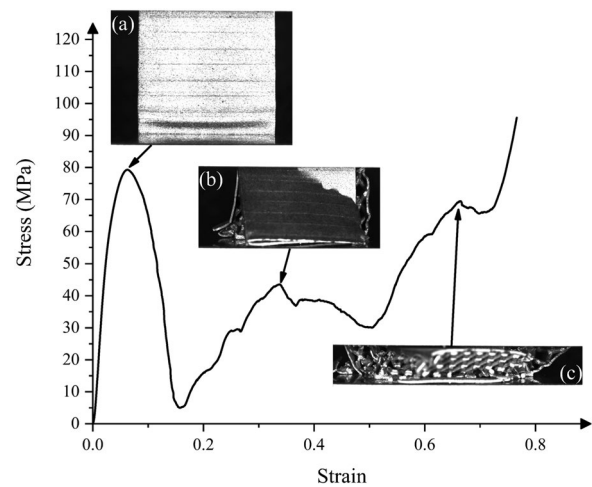
positions, the experimental results were almost the same as those of the sample with a 1.0-mm strut diameter. After the exterior shells tear, the frontal exterior shells completely lose their load-bearing capabilities, as demonstrated in Figure 14(b). In Figure 14(c), all the exterior shells at the third stress peak expand outward; thus, the interior BCC lattice structure changes to the main load-bearing structure. When the lattice is crushed, the entire structure enters the densification stage.

3.4 Comparison Discussions

Figure 15 compares the quasi-static compressive experimental results for different strut diameters in terms of the stress-strain curve and specific energy absorption
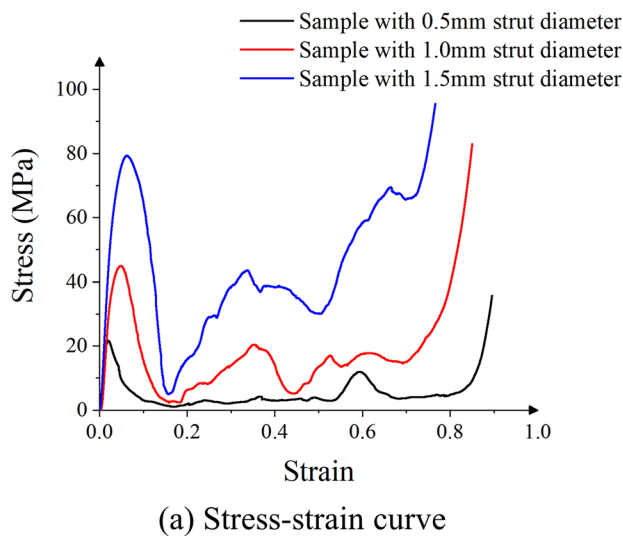
(a) Stress-strain curve
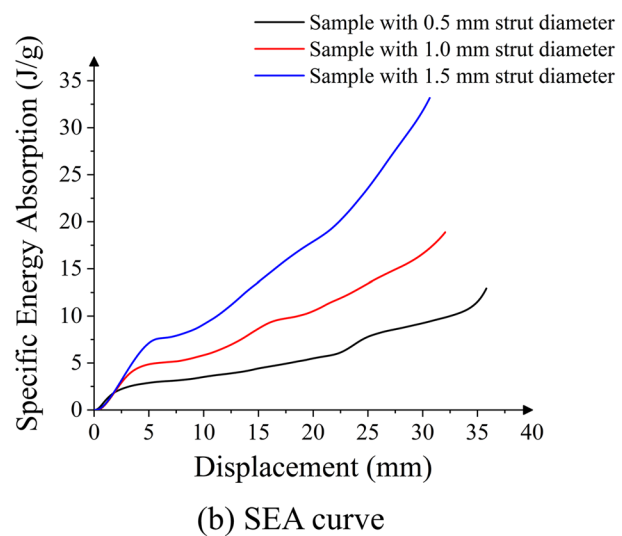
(b) SEA curve

Figure 15 Comparison of quasi-static experiments with different strut diameter

Bai *et al. Chinese Journal of Mechanical Engineering*   (2023) 36:143

Page 8 of 13

Table 2 Mechanical parameters of the samples

Strut diameter (mm)	0.5	1.0	1.5
Effective Young's modulus (MPa)	1711.57	2175.58	2688.53
Specific modulus (MPa/g)	66.49	48.01	38.57
Ultimate strength (MPa)	21.65	44.94	79.31
SEA (J/g)	12.94	18.88	33.17

(SEA). The stress-strain curves share a similar changing trend with three stages: elastic, nonlinear damage, and densification. In addition, increasing the strut diameter significantly strengthened the load-carrying capacity of the entire structure. Table 2 presents the corresponding mechanical properties and energy absorption indicator (SEA) results. The effective Young's modulus increases by 57%, from 1711.57 to 2688.53 MPa, with increasing strut diameter. In terms of energy absorption, the SEA exhibited a 156% increase from 12.94 to 33.17 J/g.

Furthermore, selected deformation values are provided in Table 3 for samples with different strut diameters.

The shell-infill structure with thinner struts reached the maximum stress at a smaller strain; however, the initial tearing of the exterior shells occurred at a similar strain. The first tearing between the adjacent shells of the sample with a 0.5-mm strut diameter occurred in the middle of the structure, which was very different from that of the other samples. Therefore, the internal BCC structure can extend the elastic phase and increase the peak stress. With an increase in loading, the deformation mode of the BCC structure determines the collapse trend of the exterior shells, in which the coupling effect of the exterior shells and interior infill plays a very important role.

4 Finite Element Analysis and Discussions
4.1 Modeling Strategy Selection Based on Quasi-static Compression Analysis

Because of their large geometric and material gradients, numerical simulations are challenging. This section compares the beam-shell type and solid element models to determine an appropriate model for the mechanical properties. The stress-strain curves of the corresponding experiments, beam-shell simulation

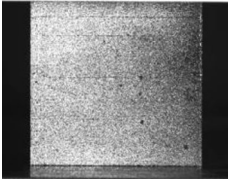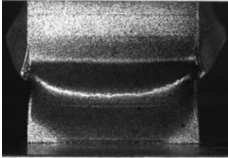**Table 3** Deformation comparison of compressive experiments
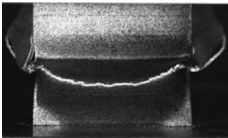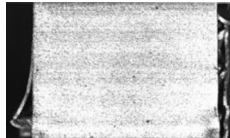
Selected deformation time	Strut diameter (mm)		
	0.5	1.0	1.5
Strain of max stress	$\varepsilon = 0.020$	$\varepsilon = 0.048$	$\varepsilon = 0.062$
Strain of first damage	$\varepsilon = 0.112$	$\varepsilon = 0.099$	$\varepsilon = 0.111$
Strain of first tearing between adjacent shells	$\varepsilon = 0.174$	$\varepsilon = 0.144$	$\varepsilon = 0.148$

Bai *et al. Chinese Journal of Mechanical Engineering*   (2023) 36:143

Page 9 of 13

Table 4 Stress–strain curve of experimental and simulation results

Strut diameter (mm)	Experimental and beam-shell simulation results	Experimental and solid element simulation results
0.5		
1.0		
1.5		
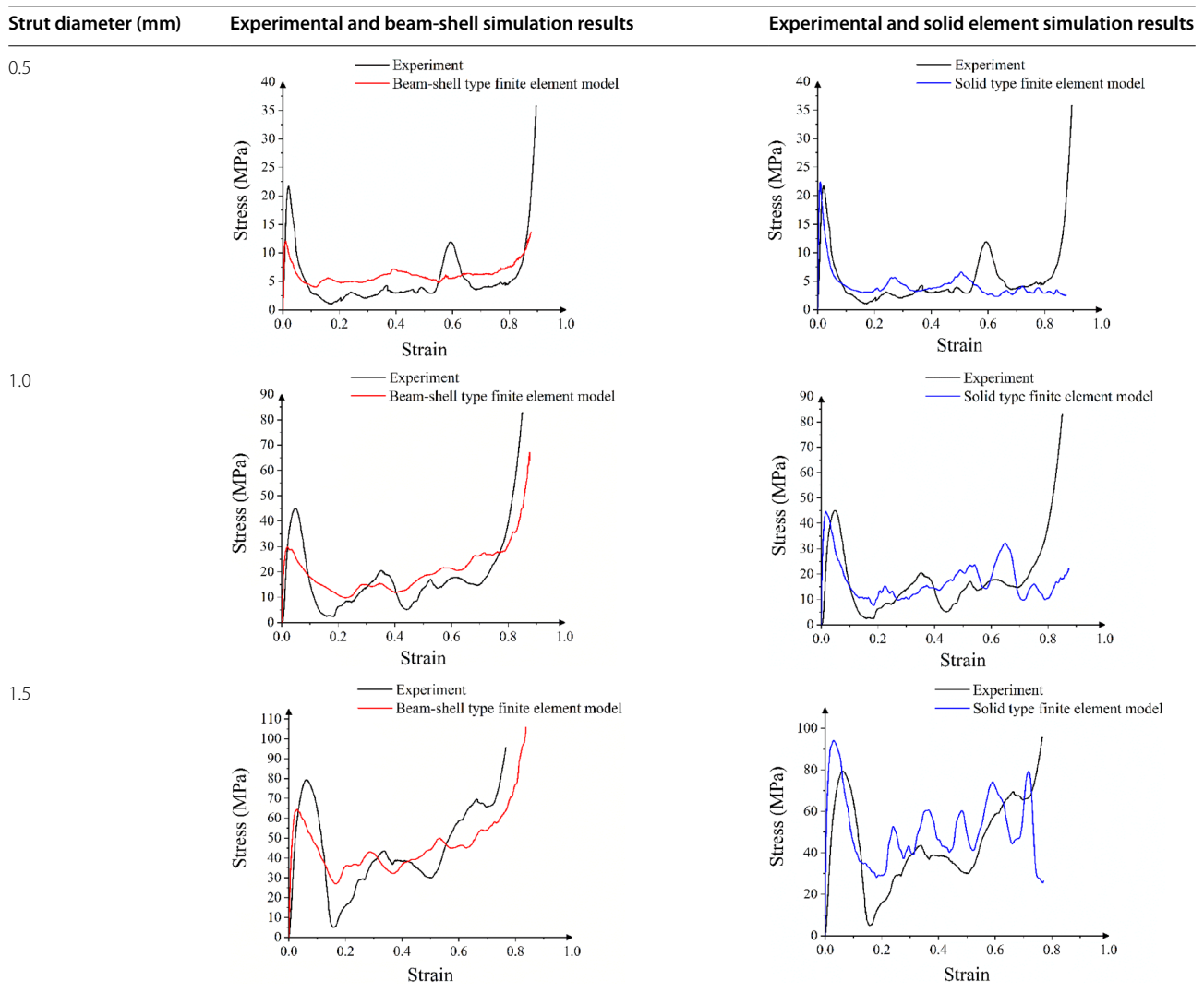
results, and solid element simulation results are presented in Table 4. The beam-shell model can predict the three stages more accurately than the solid element model. For the solid element model, element deletion was added to guarantee the stress-strain curve trend. However, the resulting penetration led to stress

Table 5 Comparison of effective Young's modulus between finite element analysis models and experiments (MPa)

Strut diameter (mm)	Experiment	Beam-shell type simulated results	Solid element type simulated results	
0.5	1711.10	1696.23 (0.87%)	2542.01	48.56
1.0	2175.58	2379.18 (9.36%)	3804.19	74.86
1.5	2688.53	2909.74 (8.23%)	6702.79	149.31

fluctuations during compression. The effective Young's moduli for both the experiments and simulations are presented in Table 5. The simulation results obtained using the beam-shell model were closer to the experimental values compared to those obtained using the solid element model.

In addition, the deformations of both experiments and two types of finite element simulations of the sample with a 1.0-mm strut diameter are shown in Table 6. The deformation of the beam-shell type model is more accurate, especially for the exterior shells. As the strain is within the range of 0.2–0.3, prediction results by the beam-shell type model are more accurate than those by the solid-type model. The deformation results of the solid element model revealed that the internal lattice distribution largely affected the deformation of the model's overall structure. The stress distribution is

Table 6 Deformation comparison between experiments and finite element models with 1.0-mm strut diameter

Strain	Experiment results	Beam-shell model simulation results	Solid element model simulation results
0.1			
0.2			
0.3			
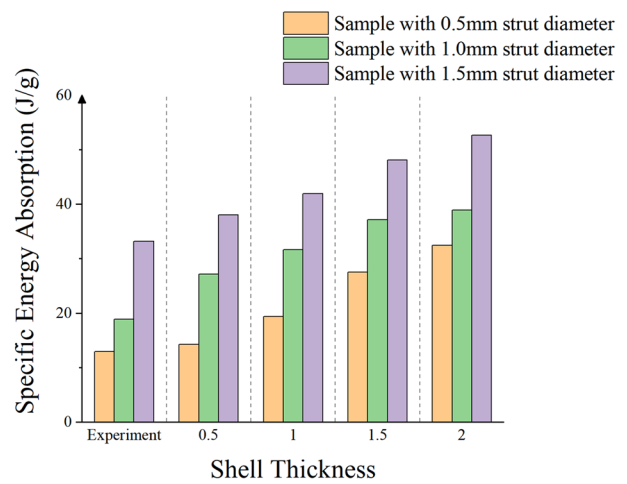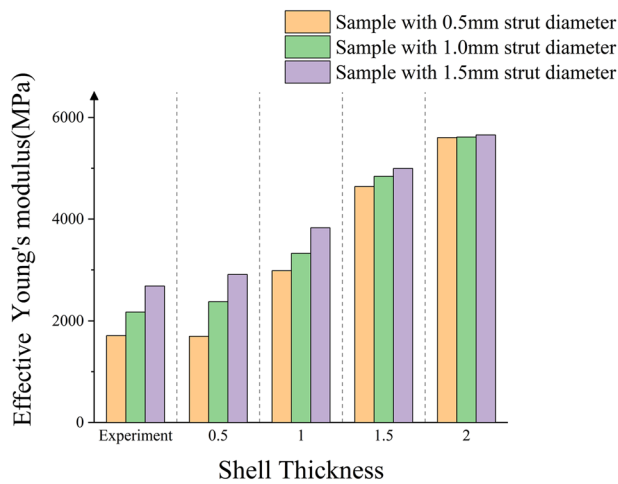
(a) Effective Young's modulus

(b) Specific energy absorption

Figure 16 Mechanical performances comparison with different geometric parameters (shell thickness and strut diameter)

consistent with the spatial arrangement of the filling structure. Based on the above comparison, the beam-shell type modeling strategy is the most appropriate for shell structures with BCC lattice infills.

4.2 Effects of Shell Thickness on Mechanical Performances

Based on the beam-shell modeling strategy, quasi-static compressive numerical simulations for shell thicknesses of 0.5, 1.0, 1.5, and 2.0 mm were performed with three

Table 7 Comparison of deformation modes between shell-infill structure and lattice structure

Strain	Deformation process		
	Shell-infill structure		Lattice structure
	Axonometric view	Cross-sectional view	
0.2			
0.3			
0.4			
0.5			

different strut diameters to investigate their effects on mechanical performance. The corresponding effective Young's moduli and SEA are compared in Figure 16. The increase in shell thickness improved the effective Young's modulus and SEA, particularly for lattice infills with smaller diameters. This is because the exterior shell was the main load-carrying structure during the early deformation stage. The effective Young's modulus for a shell thickness of 2.0 mm can reach 3.3 times that for a shell thickness of 0.5 mm. It can also be observed that the effective Young's modulus exhibits a larger difference for structures with thinner shells when the strut diameter is changed.

By contrast, there are fewer differences with a thicker exterior shell. For the SEA, both the exterior shell and the lattice infill contribute to the structural energy absorption capability through plastic deformation. Increasing the shell thickness and strut diameter can improve the energy absorption. Changing the strut diameter could improve the energy absorption by almost 1.7 times because the plastic deformation of lattice infill can absorb more energy than the exterior shells.

4.3 Comparison of Shell-infill Structure and Lattice Structure

In this section, we discuss the results of quasi-static compression simulations of a pure BCC lattice structure
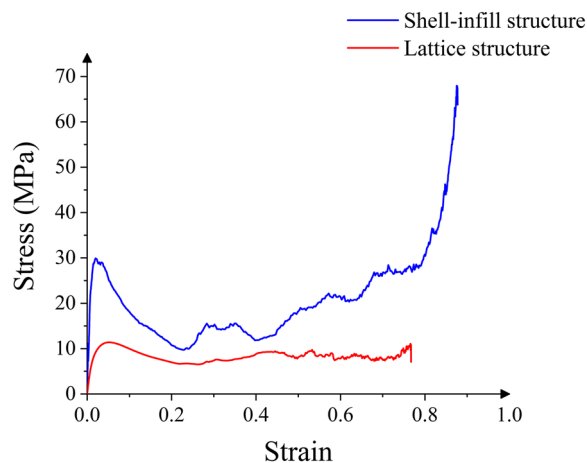
Bai *et al. Chinese Journal of Mechanical Engineering*   (2023) 36:143

Page 12 of 13

Figure 17 Stress-strain curve of shell-infill structure and lattice structure

containing only beam elements that were performed to investigate the effect of shell structures on the overall behavior and deformation modes. The differences in the stress-strain curves between a BCC-infilled shell structure and a pure BCC structure are illustrated in Figure 17. The stress of the shell-infill structure was much higher than that of the pure lattice structure, which gave the shell structure a significant strengthening effect on its overall structure. The maximum stress of the shell-infilled structure was twice that of the pure lattice structure, leading to improved energy-absorbing capabilities. However, the buckling deformation of the exterior shell significantly reduced the load-carrying capacity. Meanwhile, the outward buckling of the shell generated self-contact and contact with the infill, causing stress fluctuations. However, the stress-drop amplitude of the pure lattice structure after the elastic stage was small, and the yield stage was relatively stable.

Table 7 presents a comparison of the deformation modes of the shell BCC filling structure and the pure lattice structure. The shell structure has an important impact on the deformation mode of the infill structure. The shear bands of both the BCC-infilled shell structures and pure BCC structures generally expand along their diagonals. In addition, the positions of the shear bands are different owing to the coupling effect of the exterior shell and in-filled lattice.

5 Conclusions

We investigated the mechanical properties and energy absorption of shell structures with a BCC lattice infill by AM.

(1) Compression tests of the integrated AlSi10Mg additively manufactured samples demonstrated that the strut diameter significantly influences the equivalent Young's modulus and specific energy absorption.

(2) Two different types of finite element construction methods were systematically investigated: the beam-shell element model and the solid element model. Based on a comparison with experimental results, the beam-shell element model is found to be more appropriate for shell-infill structure modeling for quasi-static analysis in terms of the effective Young's modulus and SEA.

(3) The effects of shell thickness were further analyzed for the effective Young's modulus and SEA, in which the shell thickness contributed largely to the effective Young's modulus. By contrast, the strut diameter contributed largely to the SEA.

(4) The pure lattice structure was numerically compared with the BCC-filled shell structure, and the influence of the shell structure on the mechanical response and deformation mode of the overall structure was analyzed. The result shows that the shell structure had a significant strengthening effect on its overall structure.

Authors' Contributions
YB contributed to write and revise the manuscript, and supervise this research project. JG processed data and wrote the manuscript; CH conducted the experiments and simulation, and wrote the manuscript. YL contributed to the revision of the manuscript. All authors read and approved the final manuscript.

Authors' Information
Yingchun Bai born in 1987, is an associate professor and a PhD candidate supervisor at *National Engineering Research Center of Electric Vehicles, Beijing Institute of Technology, China*. His research interests include advanced design methodologies and applications of new-energy vehicles and high-end equipment.
Jiayu Gao born in 1998, is currently a master candidate at *National Engineering Research Center of Electric Vehicles, Beijing Institute of Technology, China*.
Chengxiang Huang born in 1998, is a master candidate at *National Engineering Research Center of Electric Vehicles, Beijing Institute of Technology, China,* in 2022.
Yue Li born in 1987, is currently a visiting scholar at *National Engineering Research Center of Electric Vehicles, Beijing Institute of Technology, China*.

Availability of data and materials
The datasets used and/or analyzed in the current study are available from the corresponding author on reasonable request.

Declarations

Competing interests

The authors declare that they have no known competing financial interests or personal relationships that could have appeared to influence the work reported in this paper.

References

[1] J Choe, Q Huang, J Yang, et al. An efficient approach to investigate the post-buckling behaviors of sandwich structures. *Composite Structures*, 2018, 201: 377-388.

[2] I Flores, N Kretzschmar, A H Azman, et al. Implications of lattice structures on economics and productivity of metal powder bed fusion. *Additive Manufacturing*, 2020, 31: 100947.

[3] J Nguyen, S Park, D Rosen. Heuristic optimization method for cellular structure design of light weight components. *International Journal of Precision Engineering and Manufacturing*, 2013, 14: 1071-1078.

[4] Y Bai, W Jing. Multiscale topology optimization method for shell-infill structures based on filtering/projection boundary description. *Journal of Mechanical Engineering*, 2021, 57: 121-129. (in Chinese)

[5] X Chen, C Li, Y Bai. Topology optimization of sandwich structures with solid-porous hybrid infill under geometric constraints. *Computer Methods in Applied Mechanics and Engineering*, 2021, 382: 113856.

[6] V-N Hoang, X Wang, H Nguyen-Xuan, A three-dimensional multiscale approach to optimal design of porous structures using adaptive geometric components. *Composite Structures*, 2021, 273: 114296.

[7] X Li. *Study on the buffering and energy-absorbed property of combined hexagonal aluminum honeycomb.* Changsha: National University of Defense Technology, 2016. (in Chinese)

[8] J Zhang. *Design and investigation of dynamic crushing of graded lattice cylindrical shell structure.* Chongqing: Chongqing University, 2018. (in Chinese)

[9] C Zeng, L Liu, W Bian, et al. Compression behavior and energy absorption of 3D printed continuous fiber reinforced composite honeycomb structures with shape memory effects. *Additive Manufacturing*, 2021, 38: 101842.

[10] C Zeng, L Liu, W Bian, et al. Bending performance and failure behavior of 3D printed continuous fiber reinforced composite corrugated sandwich structures with shape memory capability. *Composite Structures*, 2021, 262: 113626.

[11] D Muchhala, B Yadav, A Pandey, et al. Influences of relative density and strain rate on the mechanical properties of Al-cenosphere-SWNTs hybrid foams. *International Journal of Mechanical Sciences*, 2021, 198: 106388.

[12] B Vengatachalam, R Huang, L H Poh, et al. Initial yield behaviour of closed-cell aluminium foams in biaxial loading. *International Journal of Mechanical Sciences*, 2021, 191: 106063.

[13] A Cherniaev. Modeling of hypervelocity impact on open cell foam core sandwich panels. *International Journal of Impact Engineering*, 2021, 155: 103901.

[14] Y Hu, W Li, H Fan, et al. Experimental investigations on the failures of woven textile sandwich panels. *Journal of Thermoplastic Composite Materials*, 2017, 30: 196-224.

[15] B Wang, S Zhu, P Hao, et al. Buckling of quasi-perfect cylindrical shell under axial compression: a combined experimental and numerical investigation. *International Journal of Solids and Structures*, 2018, 130: 232-247.

[16] B Wang, K Du, P Hao, et al. Experimental validation of cylindrical shells under axial compression for improved knockdown factors. *International Journal of Solids and Structures*, 2019, 164: 37-51.

[17] D Gu, X Shi, R Poprawe, et al. Material-structure-performance integrated laser-metal additive manufacturing. *Science*, 2021, 372: 1487.

[18] L-Y Chen, S-X Liang, Y Liu, et al. Additive manufacturing of metallic lattice structures: Unconstrained design, accurate fabrication, fascinated performances, and challenges. *Materials Science and Engineering: R: Reports,* 2021, 146: 100648.

[19] M B Kumar, P Sathiya, Methods and materials for additive manufacturing: A critical review on advancements and challenges. *Thin-Walled Structures*, 2021, 159: 107228.

[20] J Plocher, A Panesar, Review on design and structural optimisation in additive manufacturing: Towards next-generation lightweight structures. *Materials & Design*, 2019, 183: 108164.

[21] T Maconachie, M Leary, B Lozanovski, et al. SLM lattice structures: Properties, performance, applications and challenges. *Materials & Design*, 2019, 183: 108137.

[22] C Peng, P Tran, H Nguyen-Xuan, et al. Mechanical performance and fatigue life prediction of lattice structures: Parametric computational approach. *Composite Structures*, 2020, 235: 111821.

[23] P Li. Constitutive and failure behaviour in selective laser melted stainless steel for microlattice structures. *Materials Science and Engineering: A*, 2015, 622: 114-120.

[24] M Smith, W Cantwell, Z Guan, et al. The quasi-static and blast response of steel lattice structures. *Journal of Sandwich Structures & Materials*, 2011, 13: 479-501.

[25] S Merkt, C Hinke, J Bültmann, et al. Mechanical response of TiAl6V4 lattice structures manufactured by selective laser melting in quasistatic and dynamic compression tests. *Journal of Laser Applications*, 2015, 27: S17006.

[26] I Maskery, N Aboulkhair, A Aremu, et al. A mechanical property evaluation of graded density Al-Si10-Mg lattice structures manufactured by selective laser melting. *Materials Science and Engineering: A*, 2016, 670: 264-274.

[27] V Sufiiarov, V Sokolova, E Borisov, et al. Investigation of accuracy, microstructure and properties of additive manufactured lattice structures. *Materials Today: Proceedings*, 2020, 30: 572-577.

[28] Y Xu, D Zhang, S Hu, et al. Mechanical properties tailoring of topology optimized and selective laser melting fabricated Ti6Al4V lattice structure. *Journal of the Mechanical Behavior of Biomedical Materials*, 2019, 99: 225-239.

[29] D Kang, S Park, Y Son, et al. Multi-lattice inner structures for high-strength and light-weight in metal selective laser melting process. *Materials & Design*, 2019, 175: 107786.

[30] C Li, H Lei, Y Liu, et al. Crushing behavior of multi-layer metal lattice panel fabricated by selective laser melting. *International Journal of Mechanical Sciences*, 2018, 145: 389-399.

[31] A Clausen, E Andreassen, O Sigmund. Topology optimization of 3D shell structures with porous infill. *Acta Mechanica Sinica*, 2017, 33: 778-791.

[32] E Cetin, C Baykasoğlu. Energy absorption of thin-walled tubes enhanced by lattice structures. *International Journal of Mechanical Sciences*, 2019, 157: 471-484.

[33] A Baykasoğlu, C Baykasoğlu, E Cetin. Multi-objective crashworthiness optimization of lattice structure filled thin-walled tubes. *Thin-Walled Structures*, 2020, 149: 106630.

[34] E Cetin, C Baykasoğlu. Crashworthiness of graded lattice structure filled thin-walled tubes under multiple impact loadings. *Thin-Walled Structures*, 2020, 154: 106849.

[35] H Liu, Z X C Chng, G Wang, et al. Crashworthiness improvements of multi-cell thin-walled tubes through lattice structure enhancements. *International Journal of Mechanical Sciences*, 2021, 210: 106731.

[36] A Clausen, N Aage, O Sigmund. Exploiting additive manufacturing infill in topology optimization for improved buckling load. *Engineering*, 2016, 2: 250-257.

[37] R Schwab, A Harter. Extracting true stresses and strains from nominal stresses and strains in tensile testing. *Strain,* 2021, 57: 12396.